3D Fuzzy Graphene Microelectrode Array for Neurotransmitter Sensing at Sub-cellular Spatial Resolution

Elisa Castagnola[1], Raghav Garg[2], Sahil K. Rastogi[3], Tzahi Cohen-Karni[2,3,4,], Xinyan Tracy Cui[1,4,5,*]*

[1] Department of Bioengineering, University of Pittsburgh, 3501 Fifth Avenue, Pittsburgh, PA 15260, USA.

[2] Department of Materials Science and Engineering, Carnegie Mellon University, 5000 Forbes Avenue, Pittsburgh, PA, 15213, USA.

[3] Department of Biomedical Engineering, Carnegie Mellon University, 5000 Forbes Avenue, Pittsburgh, PA, 15213, USA.

[4] McGowan Institute for Regenerative Medicine, University of Pittsburgh, 450 Technology Drive Pittsburgh, PA 15219-3110, USA

[5] Center for Neural Basis of Cognition, University of Pittsburgh, 4400 Fifth Ave, Pittsburgh, PA 15213, USA.

*corresponding authors: Tzahi Cohen-Karni (tzahi@andrew.cmu.edu), X. Tracy Cui (xic11@pitt.edu)

Keywords: 3D graphene, microelectrode arrays (MEAs), dopamine, neurotransmitters, fast scan cyclic voltammetry, electrochemical sensing.

Abstract:

Dopamine (DA) is a monoamine neurotransmitter involved in the modulation of various physiological brain functions, including learning, motivation, reward, and motor functions. The development of a high sensitivity real-time sensor for multi-site detection of DA with high spatial resolution has critical implications for both neuroscience and clinical communities to improve understanding and treatments of neurological and neuropsychiatric disorders. Here, we present high-surface area out-of-plane grown three-dimensional (3D) fuzzy graphene (3DFG) microelectrode arrays (MEAs) for highly selective, sensitive, and stable DA electrochemical sensing. 3DFG microelectrodes present a remarkable sensitivity to DA (2.87 ± 0.25 nA/nM, with LOD of 990 ± 15 pM), the highest reported for nanocarbon MEAs using Fast Scan Cyclic Voltammetry (FSCV). The high surface area of 3DFG allows for miniaturization of electrode down to 2×2 μm^2, without compromising the electrochemical performance. Moreover, 3DFG MEAs are electrochemically stable under 7.2 million scans of continuous FSCV cycling, present exceptional selectivity over the most common interferents *in vitro* with minimum fouling by electrochemical byproducts, and can discriminate DA and serotonin (5-HT) in response to the injection of their 50:50 mixture. These results highlight the potential of 3DFG MEAs as a promising platform for FSCV based multi-site detection of DA with high sensitivity, selectivity, and spatial resolution.

1. Introduction

Dopamine (DA) is a monoamine neurotransmitter involved in the modulation of various physiological brain functions, including learning, motivation, reward, and motor functions (Arias-Carrión and Pöppel 2007; Schultz 2007; Wise 2004). Imbalance in the physiological concentration of DA is related to many neurological disorders, such as Parkinson's disease, schizophrenia, and drug addiction (Ahlskog 2007; Brisch et al. 2014; Gründer and Cumming 2016; Höglinger et al. 2004; Lotharius and Brundin 2002; Si and Song 2018; Volkow et al. 2011). It is well known that the DA release has region specificity, thus, the development of a high sensitivity real-time sensor for multi-site detection of DA with high spatial resolution has critical implications for both neuroscience and clinical communities to improve understanding and treatments of neurological and neuropsychiatric disorders.

For the last 3 decades, carbon fiber electrodes (CFEs) under fast scan cyclic voltammetry (FSCV) have been considered the gold standard for *in-vivo* DA detection (Ou et al. 2019; Puthongkham and Venton 2020). When used in combination with behavioral and/or pharmacological paradigms, this technique has provided groundbreaking knowledge on the molecular mechanisms underlying particular aspects of goal-driven action and associative learning.(Howe et al. 2013; Phillips et al. 2003; Roitman et al. 2004; Stouffer et al. 2015) However, FSCV measurements with CFEs are usually limited to one electrode site at a time, while the DA release dynamic is complex and differs in different brain regions or different loci of the same region (Owesson-White et al. 2009; Puthongkham and Venton 2020), requiring high resolution multisite measurements in order to understand its spatial and temporal pattern. Additionally, selectivity of CFE for DA over other electrochemical species has been suboptimal. Furthermore CFEs are subjected to electrochemical fouling due to carbon degradation or electrochemical byproduct deposition when exposed to brain

tissue, which results in diminished sensing capabilities over time (Harreither et al. 2016; Hensley et al. 2018; Mohebi et al. 2019; Puthongkham and Venton 2020). To develop *in-vivo* robust neurotransmitter sensing paradigms, including high spatial resolution sensing, multisite measurements, simultaneous detection of different neurotransmitters, and multimodality integration, these limitations must be resolved.

In recent years, various strategies have been explored to overcome some of these limitations. For example, to enable multi-site high spatial resolution DA sensing, CFE arrays have been fabricated and successful DA detection has been demonstrate, both in acute and chronic studies (Schwerdt et al. 2017; Schwerdt et al. 2018). However, their fabrication process is semi-manual, which is a bottle-neck for batch-fabrication and scaled up production of high density electrodes with a 3D arrangement. On the other hand, to further improve their sensitivity, CFEs have been coated with different edge plane-rich, sp^2-hybridized carbon nanomaterials, i.e. carbon nanotubes (CNTs)(Puthongkham and Venton 2020; Swamy and Venton 2007a), carbon nanohorns (CNHs),(Puthongkham et al. 2018) and graphene oxide nanosheets alone or as composite with conducting polymers (Taylor et al. 2017). Such hybrid electrodes demonstrate different degrees of improvements in sensitivity and detection limits along with enhanced antifouling properties.(Puthongkham and Venton 2020; Puthongkham et al. 2018) However, the stability of the coatings is a potential limitation towards chronic sensing of neurotransmitters.

So far, only a handful of efforts have been documented in literature for batch-fabrication of carbon or nanocarbon-based microelectrode arrays (MEAs) using well-established microfabrication techniques. For example, 4-channel arrays of pyrolyzed glassy carbon (GC) on silicon substrate (Zachek et al. 2010), and polyimide substrates (Castagnola et al. 2018) were used for DA sensing. Despite their success in multisite *in-vivo* DA detection under FSCV (Zachek et al. 2010), and their

superior DA sensitivity compared to CFEs (Zachek et al. 2010), GC exhibits a smooth surface topography with limited electrochemical surface area, rendering further miniaturization difficult (El Merhie et al. 2018; Goshi et al. 2018; Pancrazio et al. 2017; Vomero et al. 2017). Graphene-based MEAs have been fabricated for simultaneous recordings of the electrophysiology and Ca^{2+} signaling in electrogenic cells (El Merhie et al. 2018; Liu et al. 2019; Lu et al. 2018; Rastogi et al. 2018).However, they have not been widely investigated for FSCV detection in their basal planes configuration. The introduction of defects to graphene has been shown to enhance DA and serotonin (5-HT) adsorption and consequently increase detection sensitivity using FSCV,(Cao et al. 2019; Puthongkham and Venton 2020) making defect-rich graphene an attractive candidate for FSCV detection.

Here, we present a high-surface area MEA platform composed of 3D fuzzy graphene (3DFG) for neurotransmitter detection. We synthesized 3DFG using a highly controlled catalyst-free bottom-up scheme which enables tight control over the material's structure. The tunability of the 3DFG flake density and size allows highly controlled electrochemical response.(Garg et al. 2017; San Roman et al. 2020) 3DFG's enormous surface area allows miniaturization of the electrode footprint down to ca. 2 x 2 μm^2, which can enable densely packed MEAs. We characterized the electrochemical performance and sensitivity to DA of 3DFG microelectrodes with different sizes (2 x 2 μm^2 to 50 x 50 μm^2 geometric area) and compared the performance with the current standard of CFEs. We then extensively tested the stability of the 3DFG microelectrodes with regard to their electrochemical and DA sensing capabilities under prolonged (7.2 million) FSCV cycling. Additionally, we tested 3DFG microelectrode DA selectivity, sensitivity, and resistance to the deposition of byproducts generated by electrochemical reactions in presence of contaminants (200 μM ascorbic acid (AA), 10 μM uric acid (UA), 10 μM dihydroxyphenylacetic acid (DOPAC)) and

100 nM DA under 1 million FSCV cycles. Finally, we demonstrated the capability of 3DFG to discriminate DA and serotonin (5-HT), with and without contaminants.

2. Material and Methods

2.1 3DFG Microelectrodes fabrication

2.1.1 **Outer contacts/interconnects patterning.** A (100) Si substrate with a 600 nm wet thermal oxide (p-type, ≤0.005 Ω cm, Nova Electronic Materials Ltd., catalog no. CP02 11208-OX) was cleaned by sonication for 5 min. in acetone. It was rinsed in iso-propyl alcohol (IPA) and blow dried with N_2. The cleaned Si/SiO_2 substrate was treated with O_2 plasma. Pt outer contacts and interconnects were patterned using photolithography technique. 300 nm LOR3A (MicroChem) was spin-coated at 4000 rpm for 40 s followed by baking at 190 °C for 5 min. 500 nm Shipley S1805 (MicroChem) was then spin-coated followed by baking at 115 °C for 5 min. The resists were patterned using a mask aligner (Karl Suss MA6) followed by development for 1 min in CD26 developer (MicroChem). 5 nm Cr and 100 nm Pt were evaporated using e-beam evaporator (Kurt J. Lesker). Lift-off was performed in Remover PG (MicroChem) at 60 °C for 30 min, followed by acetone and IPA rinse.

2.1.2 **3D fuzzy graphene (3DFG) synthesis.** 3DFG was synthesized through plasma-enhanced chemical vapor deposition (PECVD) process.(Garg et al. 2017) The synthesis process was carried out at 800 °C at a total pressure of 0.5 Torr for 90 min under 50 sccm of CH_4 (5 % CH_4 in Ar, Airgas). The temperature of the furnace was ramped up to 800 °C under 100 sccm of Ar (Matheson Gas). A 50 W inductively coupled plasma (ICP) was generated using a 13.56 MHz RF power supply (AG 0313 Generator and AIT-600 RF, power supply and auto tuner, respectively, T&C Power Conversion, Inc.).The plasma was turned off after the synthesis step and the 3DFG coated substrate was rapidly cooled to room temperature under the flow of 100 sccm Ar.

2.1.3   **3DFG microelectrodes patterning.** 100 nm SiO_2 film was deposited on 3DFG coated chips using PECVD (Trion Orion) at 375 °C, 60 W power, and 900 mTorr under 75 sccm SiH_4 and 70 sccm N_2O. The SiO_2 coated samples were baked at 95 °C for 5 min followed by an O_2 plasma treatment for 1 min at 100 W. Using standard photolithography techniques 100 nm Cr hard mask was patterned in the shape of the 50, 5 and 2 μm electrodes on the SiO_2 layer. SiO_2 from the regions not covered by the Cr hard-mask was etched off using reactive ion etching (RIE) (Plasma Therm 790 RIE) under 22.5 sccm CHF_3 and 16 sccm O_2 at 100 W power and 100 mTorr for 5 min. Post SiO_2 etching, 3DFG from the non-electrode regions was also etched by RIE using 16 sccm O_2 and 6 sccm Ar at 20 W power and 10 mTorr for 60 min. Post etching, Cr hard mask and the underlying SiO_2 film were etched off using Cr etchant (Transene, 1020AC) and buffered oxide etchant (BOE, Transene), respectively. Finally, the Pt interconnects and the non-recording site of the 3DFG electrodes were passivated with 2 μm SU-8 (MicroChem, SU-8 2002).

2.2   Carbon fiber microelectrode fabrication. CFEs were fabricated as previously described in (Castagnola et al. 2020; Taylor et al. 2019). Briefly, borosilicate capillaries (0.4 mm ID, 0.6 mm OD; A-M systems Inc., Sequim, WA, USA), each containing a single carbon fiber (7μm diameter, T650; Cytec Carbon Fibers LLC., Piedmont, SC, USA), were pulled to a fine tip using a vertical puller (Narishige, Los Angeles, CA, USA). The tip was sealed with epoxy (Spurr Epoxy; Polysciences Inc., Warrington, PA, USA) and the exposed fiber was cut 400 μm from the glass seal using a scalpel under an optical microscope (Szx12, Olympus). A mercury drop was placed in the barrel for electrical contact to a hookup wire (Nichrome; Goodfellow, Oakdale, PA, USA). CFEs were soaked in isopropyl alcohol (Castagnola et al. 2020; Taylor et al. 2019) (Fisher Chemical, USA) for 20 minutes prior to use.

2.3   Electrochemical Characterization. EIS were performed in PBS, applying a sine wave (10 mV RMS amplitude) onto the open circuit potential while varying the frequency from 1 to 105 Hz. EIS was carried out using a potentiostat/galvanostat (Autolab, Metrohm, USA) connected to a three-electrode electrochemical cell with a platinum counter electrode and an Ag/AgCl reference electrode. During the CV tests, the working electrode potential was swept between 1 and −1 V (vs Ag/AgCl) with a scan rate of 100 mV/s. The charge storage capacity (CSC, mC/cm^2) was calculated as CSC=(∫didt)/(geometric area) in an entire CV cycle.

2.4   Scanning electron microscopy (SEM) characterization. SEM imaging was performed using a FEI Quanta 600 field emission gun (FEG) SEM. High-resolution images (2048 x 1768 pixels) were acquired at accelerating voltages of 5-20 kV with a working distance of 5 mm.

2.5   Raman spectroscopy characterization. Raman spectroscopy was performed using NT-MDT NTEGRA Spectra with 532 nm excitation through a 100× objective. Raman spectra were acquired with 0.5 ND filter and an acquisition time of 30 s. Raman spectra was acquired from 30 points across 3 independent MEA chips.

2.6   Fast Scan Cyclic Voltammetry electrochemical detection. FSCV were performed with an EI 400 (Ensman Instruments; Bloomington, IN, USA), controlled by the CV Tar Heels LabVIEW program (CV Tar Heels v4.3, University of North Carolina, Chapel Hill, NC, USA). The headstage gain was set to 1 or 5 MΩ (depending by the electrode size). Data were analyzed using HDCV software (UNC Chapel Hill). The electrode was scanned from -0.5 to 1.3 V (vs Ag/AgCl) and back with a 400 V/s scan rate and a repetition rate of 10 Hz. DA detection was identified by inspection of background-subtracted cyclic voltammograms. Electrodes were calibrated using freshly prepared nitrogen purged 1x phosphate buffered saline (PBS), with and

without presence of interference. Electrode sensitivities were determined by the linear regression slope of the maximum faradaic current vs. DA concentration calibration plots.

3DFG selectivity has been assessed toward 200 µM ascorbic acid (AA), 10 µM uric acid (UA), usually presented in the brain at several order of magnitude higher than DA[Yang et al. 2017], 10 µM dihydroxyphenylacetic acid (DOPAC), a DA metabolite, and 100 nM of DA, similar concentration than the absolute basal DA level measured in the rat dorsal striatum in our previous study (82 ± 6 nM).(Taylor et al. 2019)

2.7 FSCV Stability tests

The 3DFG and CFE microelectrodes were cycled under FSCV experiment for at least 200 h, corresponding to 7.2 million cycles at 10Hz, using a standard triangular waveform from -0.5 to 1.3 V with 400V/s scan rate, at 10Hz in PBS. The electrode sensitivity to 1µM DA and the total background current of the microelectrodes were monitored after 0.9, 2.7, 3.6, 5.4 and 7.2 million FSCV cycles, corresponding to 25, 50, 75,100, 150 and 200 hours). The CSC was calculated as CSC=($\int$didt) / (geometric area) in an entire CV cycle.

2.8 FSCV Fouling characterization.

The fouling test consists in continuous FSCV cycling (triangular waveform -0.5 to 1.3 V with 400V/s scan rate, at 10Hz) of the 3DFG microelectrodes and CFEs for 24 h (corresponding to 1 million FSCV scans) in 1x PBS containing 200 µM AA, 10 µM UA, 10 µM DOPAC, and 100 nM DA. The electrode sensitivity in response to a bolus injection of 1µM DA was monitored at different timepoints (0, 0.1, 0.4, 1 million FSCV cycling).

2.9 Statistical analyses.

Statistical analyses were conducted using Origin Pro 8.1 (OriginLab Corp, Northampton, MA, USA).

One-way repeated measures ANOVA with Bonferroni post-tests was used to calculate 1) changes in the sensitivity of CFEs and 3DFG microelectrodes to DA at different time point (0, 0.9 million, 2.7, 3.6, 5.4 and 7.2 million FSCV cycles) under prolonged FSCV cycling; 2) changes in charge storage capacity (CSC, mC/cm^2) of CFEs and 3DFG microelectrodes to DA at different time point under continuous FSCV scanning; and 3) changes in the sensitivity of CFEs and 3DFG microelectrodes to DA at different time point (0, 0.1, 0.4, 1 million FSCV cycles) under prolonged FSCV cycling and in presence of interferents. Significance was determined at $p < 0.05$.

3. Results and Discussion

3DFG was synthesized by plasma enhacned chemical vapor deposition (PECVD) onto Si/SiO_2 substrates (See Materials and Methods for additional details).(Garg et al. 2017) Using standard micro- and nano-fabrication techniques, synthesized 3DFG was patterned into functional microelectrodes with sizes varying from ca. 2 x 2 μm^2 to 50 x 50 μm^2 (Supplementary Figure 1 and Supplementary Table 1; we note that misalginment during microfabrication of 3DFG led to slight deviation from the expected MEA dimensions) (Rastogi et al. 2020). The 3D topology of out-of-plane grown graphene flakes is well conserved after the MEA fabrication processes (Figure 1.A). The presence of the characteristic D (ca. 1348 cm^{-1}), G (ca. 1588 cm^{-1}), and symmetric 2D (ca. 2690 cm^{-1}) peaks in the Raman spectra confirm the presence of single-few-layer graphene flakes (Figure 1.B).(Ferrari and Basko 2013; Garg et al. 2017) The emergence of a strong D peak and the D' peak (ca. 1615 cm^{-1}), as a shoulder to the G peak, are attributed to the presence of 3DFG edges,(Ferrari and Basko 2013; Garg et al. 2017; Torrisi et al. 2012) as evident in the SEM image in Figure 1A.

We observe that the electrochemical impedance of the 3DFG MEAs decreases as the size of the MEA increases (Figure 1.C). The electrochemical impedance of 50 x 50 μm^2 3DFG MEAs is approximately an order of magnitude less than that of a carbon fiber electrode (CFE) with an area of 8830 μm^2, in particular in the low frequency range (Figure 1.C). This is attributed to the highly-exposed surface area of the 3DFG MEAs.(Rastogi et al. 2020) Over the $10–10^5$ Hz frequency domain, the 3DFG microelectrodes exhibit a near-resistive phase (approaching 0º) and an impedance modulus that is almost entirely solution resistance. At 100 Hz the impedance of the 50 x 50 μm^2 3DFG is 14-times lower (87.96 ± 5.97 kΩ versus 1.14 ± 0.16 MΩ) compared to the CFEs

impedance, while the impedance of the 10 x 10 μm^2 3DFG microelectrodes is in the same order of magnitude (2.34 ± 0.83 MΩ) of the impedance of CFE with a ca. 88-fold greater geometric area.

Cyclic voltammetry in the presence of 1x PBS presents an approximately rectangular current response in the scanned potential window (Figure 1.D), suggesting predominantly double-layer capacitance governed response during the charging and discharging process (Cogan 2008; Nimbalkar et al. 2018), with only a small reversible faradaic reaction presenting oxidation at ca. 0.2V and reduction at ca. 0 V. Furthermore 3DFG microelectrodes show a wider water window than CFEs, with no hydrolysis reactions occurring between -1V and 1 V, while CFEs present a sharp increase of water reduction current starting at -0.5 V. Furthermore, 3DFG MEAs exhibit a15-fold greater charge stroage capacity (CSC) of 15.84 ± 0.98 mC/cm2 compared to 1.05 ± 0.09 mC/cm2 of CFEs (Figure 1.D and Supplementary Figure 2). The enhaced CSC of 3DFG MEAs is attributed to the exceptionally high surface area of the material.(Cogan 2008; Rastogi et al. 2020)

These results highlight the potential of the 3DFG microelectrodes to be miniaturized without compromising the electrochemical performance, opening the possibility to fabricate high-density MEAs.
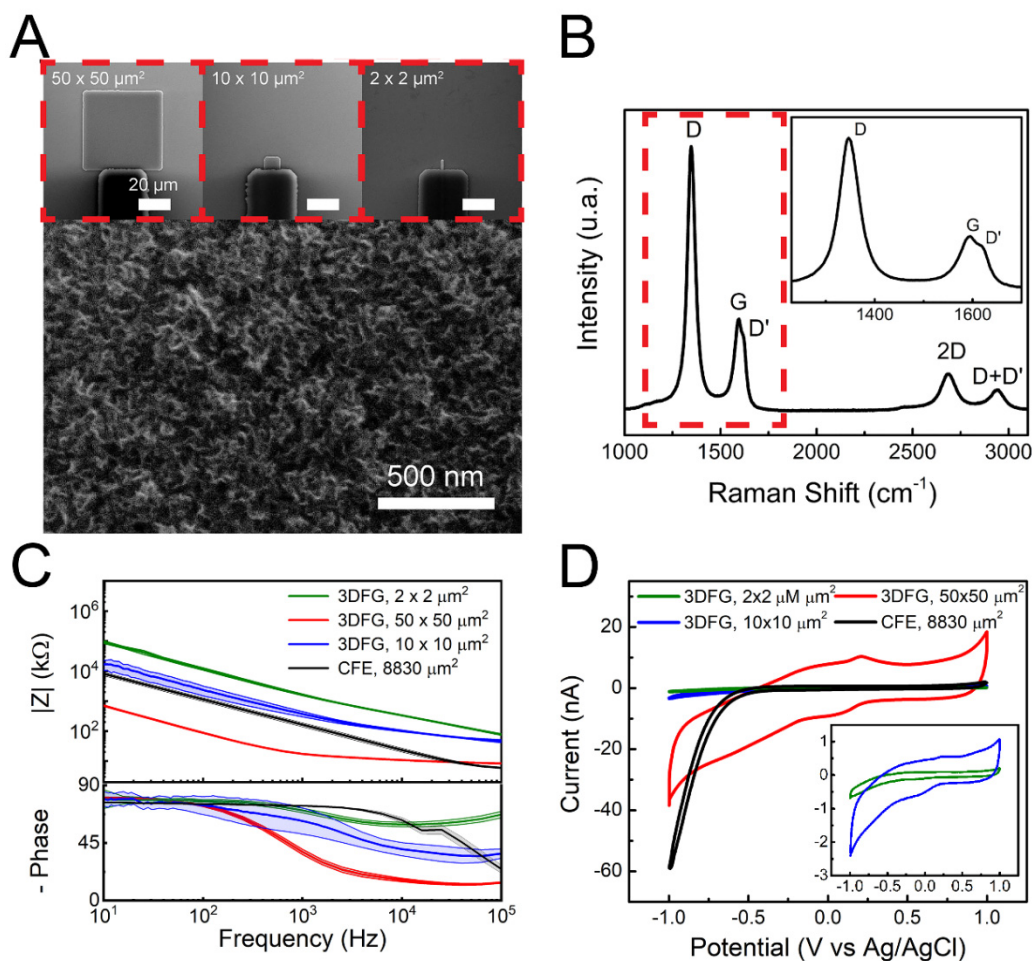
Figure 1. 3DFG morphological and electrochemical characterization. (A) Zoomed-in scanning electron microscopy (SEM) image of a 3DFG MEA. Insets present SEM images of 3DFG MEAs of varying sizes. **(B)** Raman spectra of a 3DFG microelectrode. Inset presnts expanded view of the Raman spectra marked by the red dashed box. **(C)** Impedance and negative phase as a function of frequency (mean $\pm$ sd, n =5 electrodes per size) as measured for 50 x 50 μm^2 3DFG (red), 10 x 10 μm^2 3DFG (blue), 2 x 2 μm^2 3DFG (green) MEAs, and CFEs (black) in 1x PBS. **(D)** Representative cyclic voltammograms (of 50 x 50 μm^2 3DFG (red), 10 x 10 μm^2 3DFG (blue), 2 x 2 μm^2 3DFG (green) MEAs, and CFEs (black) acquired in 1x PBS at a scan rate of 100 mV/s.

Inset presents the magnified view of the representative cyclic voltammograms of 10 x 10 μm^2 3DFG (blue), 2 x 2 μm^2 3DFG (green) plots.

DA is an electroactive compound capable of reversible oxidation to dopamine-o-quinone (DAoQ) upon application of a sufficient potential, following a two-electrons and 2 protons exchange (DA → DAoQ + 2 e$^-$ + 2 H$^+$).(Bath et al. 2000; Taylor et al. 2019; Taylor et al. 2017) DA is typically detected with FSCV through a triangular waveform with a scan rate of 400 V/s applied repeatedly at 10 Hz. The FSCV for DA usually starts from an holding potential of −0.4 V (vs. Ag/AgCl), applied to the working electrode to selectively preconcentrate cationic DA on the electrode surface,(Bath et al. 2000; Kim et al. 2018; Venton and Cao 2020) to a switching potential of +1 /+1.3V and back to the holding potential to oxidize DA and reduce DAoQ.(Puthongkham and Venton 2020; Venton and Cao 2020) While a switching potential of 1.0 V is sufficient to observe the entire DA oxidation peak,(Baur et al. 1988) scanning to potentials greater than 1.0 V has shown to increase the DA sensitivity,(Heien et al. 2003; Puthongkham and Venton 2020) due to activation of the carbon surface caused by the breaking of carbon bonds and increased exposure of the edge plane sites.(Puthongkham and Venton 2020; Takmakov et al. 2010) However, potentials above 1.3 V can etch away the carbon surface, when scanned constantly for days.(Takmakov et al. 2010) Thus, the use of 1.3 V switching potential is a good compromise for activation of the surface, while avoiding electrolysis of water(Engstrom and Strasser 1984) which could lead to electrode degradation and unstable perforamnce.(Puthongkham and Venton 2020) The use of negative holding potentials has also shown to increase the DA sensitivity, as the electrode becomes more favorable for DA adsorption;(Heien et al. 2003; Puthongkham and Venton 2020) however, below -0.5 V, oxygen reduction can occur at the CFE surface resulting in undesired

radical byproducts.(Venton and Cao 2020) As previously mentioned, 3DFG microelectrodes present a wider water window that allows for the safe use of holding potential below -0.4 V.

To evaluate the sensitivity of the 3DFG microelectrodes for DA detection in a range of concentration from 0.1 to 1 µM in PBS, we use a triangular waveform at a scan rate of 400 V/s and 10 Hz within a potential window of -0.5 V (to favor DA adsorption without incurring in oxygen reduction) to +1.3V (to activate the carbon surface while avoiding electrolysis of water). Figure 2 presents the CV traces corresponding to the detection of 0.1, 0.25, 0.5 and 1 µM bolus of DA injection after subtracting the non-faradaic capacitive charging current, for 50 x 50 µm² 3DFG and (Figure 2.A) and 2 x 2 µm² 3DFG microelectrodes (Figure 2.B), respectively. The background subtracted CVs exhibit characteristic anodic DA oxidation and cathodic DAoQ reduction peaks, confirming the detection of DA.
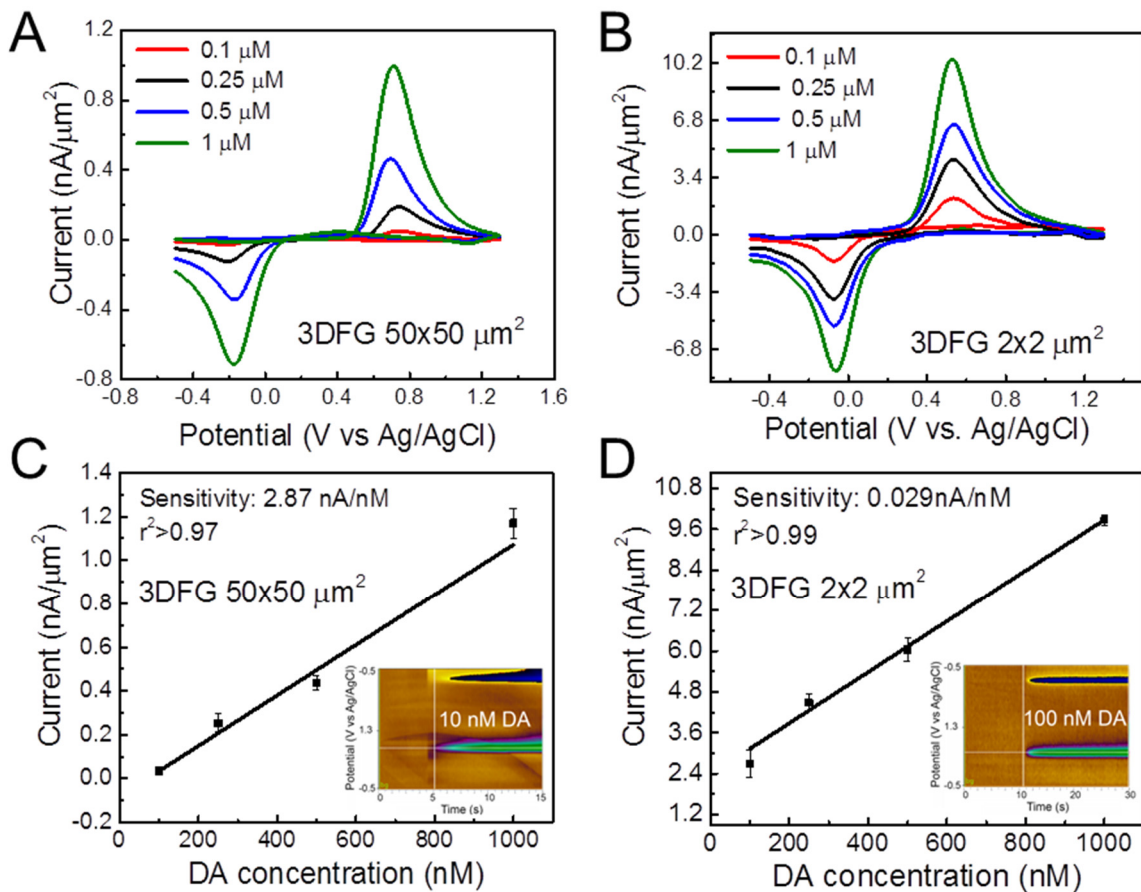
Figure 2. Dopamine sensitivity with 3DFG. Representative background subtracted FSCVs, for 0.1, 0.25, 0.5 and 1 µM bolus of DA injection collected using **(A)** 50 x 50 µm² 3DFG microelectrodes, and **(B)** 2 x 2 µm² 3DFG microelectrodes. Calibration curves – 0.1-1.0 µM concentration range- of DA in PBS using **(C)** 50 x 50 µm² 3DFG microelectrodes and **(D)** 2 x 2 µm² 3DFG microelectrodes. Inset: representative color plots for low DA concentrations:10 nM (C) and 100 nM (D), respectively.

The separation of the cathodic and anodic peaks (ΔE_p) is smaller for the miniaturized 2 x 2 µm² 3DFG electrodes ($\Delta E_p = 0.604 \pm 0.003$ V) in comparison to the 50 x 50 µm² 3DFG ($\Delta E_p = 0.892 \pm 0.021$ V), and CFEs ($\Delta E_p = 0.77 \pm 0.02$ V) indicating faster electron transfer kinetics.(Taylor et al. 2017; Yang et al. 2017) This is likely due to the small size of the miniaturized electrode that

allows for a more rapid response to changes in the applied potential.(Forster 1994, 2006) Smaller RC cell time constants and significantly reduced ohmic (iR) drop have been observed for miniaturized microelectrodes, making them very attractive for investigating high speed electron-transfer reactions.

3DFG microelectrodes sensitivity towards DA, based on the linear regression slope of maximum faradaic current versus DA concentration, is determined to be 2.87 ± 0.25 nA/nM (Mean $\pm$ SD, n=5) and 29.9 ± 1.6 nA/ μM (Mean $\pm$ SD, n=5), for 50 x 50 μm^2 and 2 x 2 μm^2 microelectrodes, respectively (Figure 2C and D). The sensitivity of 50 x 50 μm^2 3DFG microelectrodes is 220-586 fold greater than what has been reported in literature from CFEs (4.9 ± 0.5 nA/μM,(Taylor et al. 2017) and 13 ± 2 nA/μM (Vreeland et al. 2015)), 62-110 fold greater than PEDOT/Nafion CFEs (Vreeland et al. 2015) and 54-205 times higher than PEDOT/GO CFEs (Taylor et al. 2017) (Table 1). Since the sensitivity of CFEs can vary when using different FSCV waveforms, (Heien et al. 2003; Taylor et al. 2017) to have a direct comparison, we compared the DA sensitivity of CFE and 3DFG microelectrode using the same waveform (-0.5 to 1.3 V vs Ag/AgCl, 400 V/s) in the same DA concentration range (0.1 to 1 μM). 3DFG microelectrodes were found to be 33-fold more sensitive with respect to CFEs that exhibit approximately 4-times larger geometric area. Remarkably, the sensitivity of the 2 x 2 μm^2 miniaturized electrodes is still comparable to the sensitivity of CFEs with 2200-fold greater geometric area. Compared to other high surface area carbon microelectrodes, the sensitivity of 3DFG towards 1 μM DA is ca. 6-10-fold greater than CNT arrays and ca. 3-5-fold greater than CNT yarns and CNT fibers (Table 1).

The theoretical lower detection limit (LOD), defined as 3 times the standard deviation of the noise, (Harris 2010; Schmidt et al. 2013; Smith et al. 2018; Swamy and Venton 2007b; Taylor et al. 2017) was estimated to be 990 ± 15 pM (Mean $\pm$ SD, n = 5) for 50 x 50 μm^2 3DFG microelectrodes,

which is the lowest LOD value reported in literature using FSCV with carbon-based materials for DA detection (Table 1). For 2 x 2 μm^2 3DFG microelectrodes the LOD is 3.6 ± 2.2 nM (Mean ± SD, n = 4), remaining one of the lowest reported LOD value using FSCV with carbon-based materials (Table 1). Based on visual evaluation of the color plots presented in Figures 2.C and D (insets), 10 and 100 nM of DA can be physically detected, using 50 x 50 μm^2 and 2 x 2 μm^2 3DFG microelectrodes, respectively.

Table 1: DA sensing using CFE and nanocarbons (* denotes current study)

Electrode	Electrolyte	Area	LOD	Sensitivity	Sentitivity in interferent/ selectivity	Technique	Ref.
GC MEA	PBS	500 μm^2	10nM	$1.135E^{-9}$ nA/nM	1 mM AA, $1.81E^{-10}$ nA/nM	FSCV	(Nimbalkar et al. 2018)
Nanoporous CFEs	PBS	7.46 ± 1.3 μm diameter 200 μm length	35.6 nM	0.2377 nA/μM in 0-50 μM	Separation of 50 μM DA in 300μM AA	SWV	(Seven et al. 2020)
PEDOT/GO coated CFEs	aCSF	7 μm diameter, 400 μm length	0.1 μM	14-54 nA/μM	NA	FSCV	(Taylor et al. 2017)
CFEs	aCSF	7 μm diameter, 400 μm length 75 μm length	0.218 μM 20±7 nM	4.9 ± 0.5 nA/μM 13±2 nA/μM	NA	FSCV	(Taylor et al. 2017; Vreeland et al. 2015)

PEDOT/ Nafion coated CFEs	aCSF	7 μm diameter, 75 μm length	4 ± 1 nM	26 - 46 nA/μM	DA (1.0 μM), DOPAC (20 μM), AA (200 μM)	FSCV	(Vreeland et al. 2015)
CNT yarn microelectrodes (CNTYMEs)	PBS	10–25 μm	13 ± 2 nM	NA	NA	FSCV	(Yang et al. 2016b)
CNT Grown on Metal Microelectrodes and CFEs	PBS	Currents normalized for area	CNT-Nb 11±1 nM CNT-Ta 91±27 nM CNT-CFE 46 ±10 nM	CNT-Nb 197 ± 16 pA/ μm2 CNT-Ta 82 ± 10 pA/ μm2 CNT-CFE 100 ± 25 pA/ μm2 for 1μM DA	AA, DOPAC, 5-HT, adenosine and histamine	FSCV	(Yang et al. 2016a)
carbon nanospike-modified microelectrodes	PBS	Wires 100 μm lenght 25 μm dia	Ta-CNS 8 ± 2 nM Pd-CNS 27 ± 2 nM Nb-CNS 12 ± 2 nM Ni-CNS 16 ± 3 nM	Linear from 100 nM to 100 μM	UA, AA	FSCV	(Zestos et al. 2015)
Carbon nanopipettes electrodes (CNPEs)	PBS	~250 nm diameter tips, and lengths	25 ± 5 nM	linear response for DA in	serotonin, and octopamine	FSCV	(Rees et al. 2015)

		ranging from 5 to 175 μm.		0.1 to 10 μM range			
Carbon Nanohorn (CNH)modified CFME and ox-CNH/CFME	PBS pH 7.4	7 μm diameter 100 μm length	15 and 6 nM	linear response for DA in 0.05 to 5 μM range	1μM epinephrine, 1μM norepinephrine, 1 μM 5-HT, 200μM AA	FSCV	(Puthongkham et al. 2018)
3D-Printed carbon electrode and Carbon Nanoelectrodes	PBS	diameter of 65±4μm for the spheres and the hemisphere part of the cones; 288±17nm tip size	11±1 nM and 177 ± 21 nM	the DA current is linear with concentration up to 10 (micro electrode) μM and 50 μM (nanoelectrode)	1μM epinephrine, 1μM norepinephrine, 1 μM 5-HT, 200μM AA	FSCV	(Cao et al. 2020; Puthongkham et al. 2018)
CA/CNT Fiber	PBS	20 μm diameter	NA	210 ± 31 pA/μm^2 for 1μM DA	UA, AA, 5-HT	FSCV	(Yang et al. 2017)
PEI/CNT Fiber	PBS	20 μm diameter	NA	122 ± 23 pA/μm^2 for 1μM DA	UA, AA, 5-HT	FSCV	(Yang et al. 2017)
CNT Yarn	PBS	20 μm diameter	NA	290 ± 65 pA/μm^2 for 1μM DA	UA, AA, 5-HT	FSCV	(Yang et al. 2017)

3DFG microelectrodes	PBS	2500 μm^2	990±15 pM	2870 ± 250 nA/ μM	UA, AA, 5-HT	FSCV	*
3DFG miniaturized microelectrodes	PBS	4 μm^2	3.6±2.2 nM	29.9 ± 1.4 nA/ μM	UA, AA, 5-HT	FSCV	*

To evaluate the effect of a prolonged FSCV cycling on the electrochemical stability and DA sensitivity of 3DFG, we applied the FSCV waveform (-0.5 to 1.3 V vs. Ag/AgCl, scan rate: 400 V/s) at 10 Hz on the 3DFG microelectrodes in 1x PBS for over 200 h, corresponding to 7.2 million cycles, and monitored the response to 1 μM bolus injections of DA at different time points (corresponding to 0.1, 0.9, 1.8, 2.7, 3.6, 5.4, 7.2 million). As a control, and to provide a direct comparison, the same experimental protocol was applied to bare CFEs. Over 7.2 million FSCV cycles, we observe an increase in CSC for 3DFG that became significant after 2.7 million FSCV scans (Figure 3.A and B). The generation of oxygen-functional groups at the carbon surfaces under constant electrochemical FSCV cycling with a switching potential higher than 1 V (i.e. 1.3 and 1.4 V vs. Ag/AgCl) has shown to facilitate the formation of edge planes by creating strains in the lattice (Bowling et al. 1989) and it is influenced by the duration of the electrochemical cycling. We note that the G and 2D Raman peaks of the 3DFG electrodes upshift and downshift respectively after 7.2 million cycles (Supplementary Figure 3.C and Supplementary Table 2). Similar shifts, with opposite trends in the position shift of the G and 2D peaks have been observed for strained polycrystalline graphene structures with crystallite size smaller than the size of the Raman laser spot, as in the case of 3DFG.(Bissett et al. 2012; Bissett et al. 2014) This suggests the presence of increased strain in the 3DFG lattice, due to the edge plane oxygenation as a result of the strenuous FSCV cycling. For CFEs, we observed a significant decrease in CSC over time (Figure 3.C and

D). The decrease in CSC became significant after the first 0.9 million FSCV cycles and the CSC stabilized from 2.7 to 7.2 million FSCV cycles (Figure 3.C). Continuous FSCV cycling has been found to clean the electrode surface from physiosorbed impurities and alters the structure of the surface until the maximum amount of defects is formed (Bowling et al. 1989; Cao et al. 2019; Engstrom and Strasser 1984; Poon et al. 1988), at which point the electrode surface will reach a stable state. This stable surface state is likely to be reached faster at CFEs than 3DFG microelectrodes, since CFEs present lower electrochemically-active surface area. The DA sensing performance of 3DFG MEAs and CFEs did not alter as a function of FSCV cycling, since no significant difference was observed in their respective sensitivities towards DA (Figure 4).

The ratio of the peak oxidation current (anodic, $i_{p,a}$) to the peak reduction current (cathodic, $i_{p,c}$) for DA provides information about the equilibrium of absorption/desorption properties of DA and DAoQ and the reversibility of the reaction (Taylor et al. 2017; Venton and Cao 2020). We observe that the $i_{p,c}/i_{p,a}$ ratio is 0.76 ± 0.09 and 0.40 ± 0.09 for 50 x 50 μm^2 3DFG and CFEs, respectively(Cao et al. 2019; Puthongkham and Venton 2020). The increase in the cathodic DAoQ reduction peak indicates a tighter adsorption of the oxidized DAoQ towards 3DFG than CFE surfaces.(Bard and Faulkner 2001). This is similar to what was previously observed for CNT treated CFEs (Swamy and Venton 2007a), CNT fiber microelectrodes (Yang et al. 2017), and PEDOT/GO coated CFEs (Taylor et al. 2017), which share the similarity of high surface area due to the nanocarbon morphology. On CFEs, the oxidation product of DA, DAoQ, has few sites to bind to and can easily diffuse away from the smoother electrode surface when it desorbs, resulting in much lower cathodic current $i_{p,c}$ due to the low concentration of DAoQ.(Bath et al. 2000; Puthongkham and Venton 2020; Venton and Cao 2020). For 3DFG, DAoQ binding is enhanced due to the high surface area (Venton and Cao 2020; Yang et al. 2017) and DAoQ's affinity to

partially charged carbon atoms near the edge (McDermott and McCreery 1994; Taylor et al. 2017). Even if DAoQ desorbs, they may remain momentarily trapped in the three dimensional nanoporous morphology and ready to adsorb again quickly, resulting in higher $i_{p,c}$. This preconcentration effect can also act on DA and enhance DA detection on the next scan. Indeed, the electron transfer kinetics for DA oxidation has been demonstrated to be catalyzed by the adsorption of quinone containing species, including DAoQ, onto the carbon electrode surface (DuVall and McCreery 2000). This effect, combined with the greater exposed surface area, explains the enhancement in DA sensitivity (DuVall and McCreery 2000; Taylor et al. 2017).
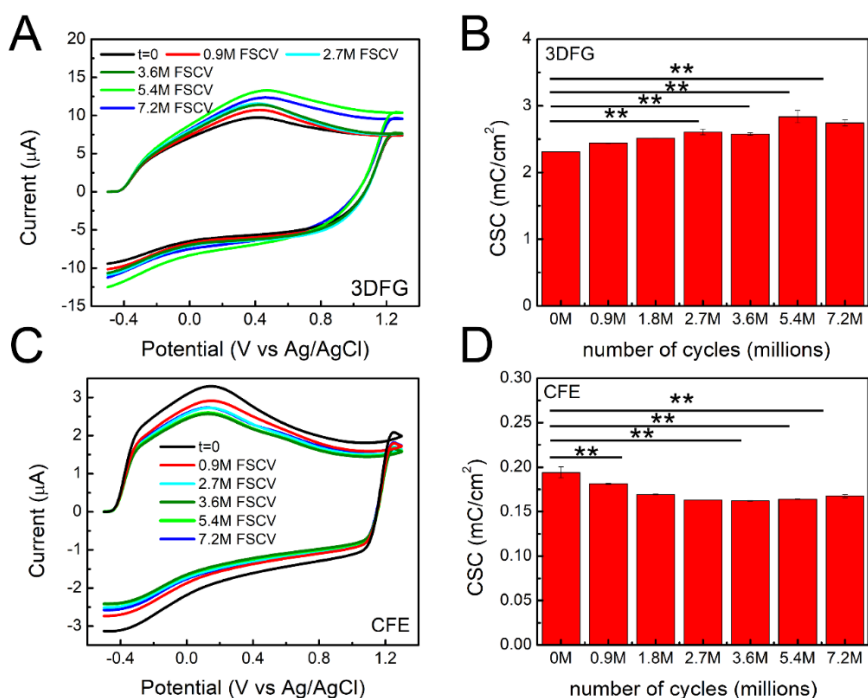

Figure 3. Electrochemical and DA sensing stability with 3DFG and CFEs. (A,B) 3DFG: (A) FSCV plots (not- background subtracted) of 50 x 50 µm² 3DFG microelectrodes at different time point (0, 0.9 million, 2.7, 3.6, 5.4 and 7.2 million FSCV cycles) (i.e. 0, 25, 75, 100, 150, 200 h) and **(B)** Column plot reporting the CSC at the different time points (average ± SEM, n=5 repetitions). (Repeated measurements ANOVA, $F_{(6,24)}=16.64209$, P=1.72052E-7 <0.05,

Bonferroni post-test** significantly different). **(C,D) CFEs: (C)** FSCV plots of CFE microelectrodes at different time point (0, 0.9 million, 2.7, 3.6, 5.4 and 7.2 million FSCV cycles) (i.e. 0, 25, 75, 100, 150, 200 h) and **(D)** Column plot reporting the CSC at the different time points (average ± SEM, n=5 repetitions). (Repeated measurements with ANOVA, $F_{(6,24)}$=21.35523, P=1.57879E-8 <0.05, Bonferroni post-hoc test** significantly different).
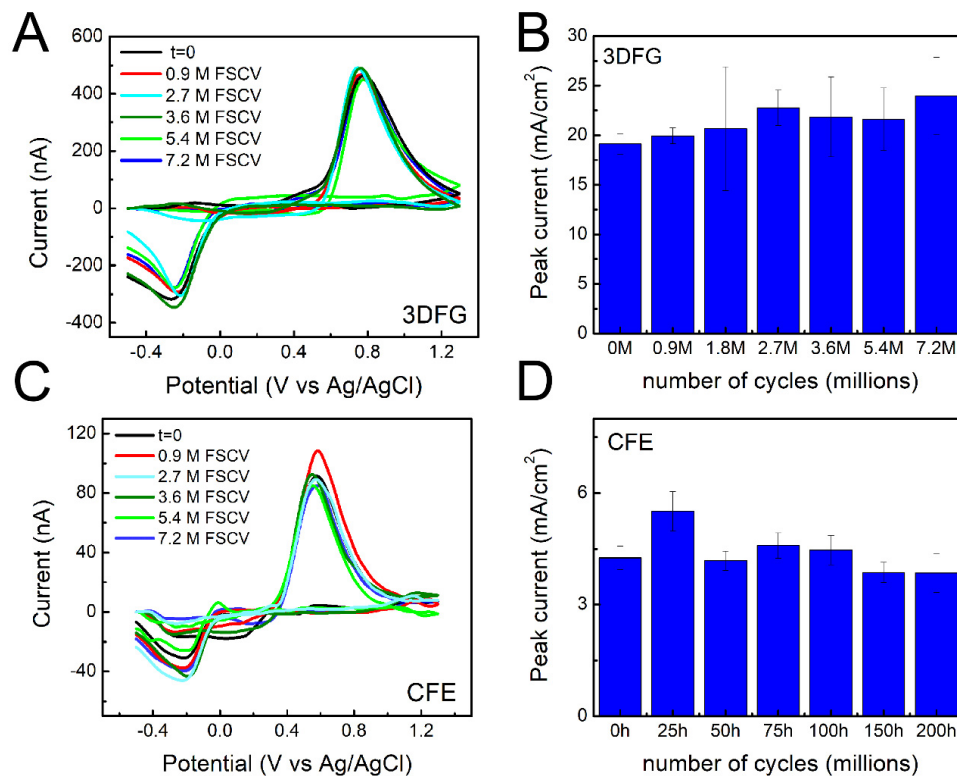

Figure 4. DA sensing stability with 3DFG and CFEs. (A,B) 3DFG: (A) Representative background subtracted CVs in response to 1μM bolus injections of DA at the time 0 and after 25, 50, 75,100, 150 and 200 hours of 3DFG FSCV continuous scanning in PBS. **(B)** Column plot reporting the amplitude of the oxidation peaks collected in response to 1μM bolus injections of DA at time zero and after 0.9, 2.7, 3.6, 5.4 and 7.2 million FSCV cycles (corresponding to 25, 50, 75,100, 150 and 200 h) of 3DFG FSCV continuous scanning in PBS. (Repeated measurements ANOVA, $F_{(6,30)}$=2.07899, P= 0.08559>0.05, Bonferroni post-hoc test ns) **(C, D) CFEs: (C)**

Representative background subtracted CVs in response to 1μM bolus injections of DA at the time 0 and after 0.9, 2.7, 3.6, 5.4 and 7.2 million FSCV cycles of CFE FSCV continuous scanning in PBS. **(D)** Column plot reporting the amplitude of the oxidation peaks collected in response to 1μM bolus injections of DA at time zero and after 0.9, 2.7, 3.6, 5.4 and 7.2 million FSCV cycles (i.e. 25, 50, 75,100, 150 and 200 h) of CFE FSCV continuous scanning in PBS. (Repeated measurements with ANOVA, $F_{(6,36)}=2.04792$, $P=0.08432>0.05$, Bonferroni post-test ns).

To assess the selectivity of the 3DFG microelectrodes towards the most common neurochemicals found throughout the complex brain environment, we characterized the DA sensing capabilities of the electrodes in presence of 200 μM ascorbic acid (AA), 10 μM uric acid (UA), 10 μM dihydroxyphenylacetic acid (DOPAC). The concentration of DA was kept constant at 100 nM since similar DA concentrations were measured in the rat's dorsal striatum using square wave voltammetry (82 ± 6 nM) (Taylor et al. 2019) and multiple cyclic square wave voltammetry (120 ± 18 nM) (Oh et al. 2018); and in the nucleus accumbens of both mice and rats, using fast scan controlled adsorption voltammetry (90 ± 9 nM) (Atcherley et al. 2015) and convolution-based FSCV(41 ± 13 nM) (Johnson et al. 2018), respectively. Our results show that 3DFG microelectrodes of 50 x 50 μm^2 (Supplementary Figure 4.A-B), 2 x 2 μm^2 (Supplementary Figure 4. C), 10 x 10 μm^2 (Supplementary Figure 4.D) geometric area can successfully detect DA in presence of interferents (Supplementary Figure 4 A-D). The sensitivity towards DA was well conserved compared to that observed for DA in 1x PBS, as observed by the background subtracted CVs of a 50 x 50 μm^2 3DFG microelectrode in response to 1 μM bolus injections of DA in 1x PBS without and with interferents (Supplementary Figure 4.A), and from the DA calibration curves of 10 x 10 μm^2 3DFG microelectrodes in 1x PBS, without and with interferents (Supplementary Figure 4.D). CFE demonstrated similar performance under interferents (Supplementary Figure 4.E

and F). However, when subjected to fouling test, 3DFG significantly outperform CFEs in preserving the DA sensitivity over time (Figure 5). The sensitivity to a bolus injection of 1 μM DA was monitored at different timepoints (0, 0.1, 0.4, and 1 million FSCV cycling). We observed that the amplitudes of DA oxidation peak did not change significantly using 3DFG microelectrodes over continuous cycling in presence of only DA (Supplementary Figure 5), and DA plus interferents (Figure 5.A and B) while were significantly diminished using CFEs (Figure 5.C and D).

The antifouling properties of the 3DFG surface may be due to the presence of various defects at their edge and electrocatalytic-active functional groups,(Hanssen et al. 2016; McCreery 2008) similarly to what previously observed for other carbon nanomaterials, such as CNT (Hanssen et al. 2016; McCreery 2008; Swamy and Venton 2007a), CNHs (Puthongkham et al. 2018), and CNT yarn microelectrode (Yang et al. 2017), when using FSCV. During the continuous cycling, the edge planes undergo oxidation that induce the formation of surface oxygen-containing groups and new defect at the graphene edge plane, that can increase the surface hydrophilicity (Garg et al. 2017) and reduce fouling (Hanssen et al. 2016; Puthongkham and Venton 2020; Yang et al. 2010).
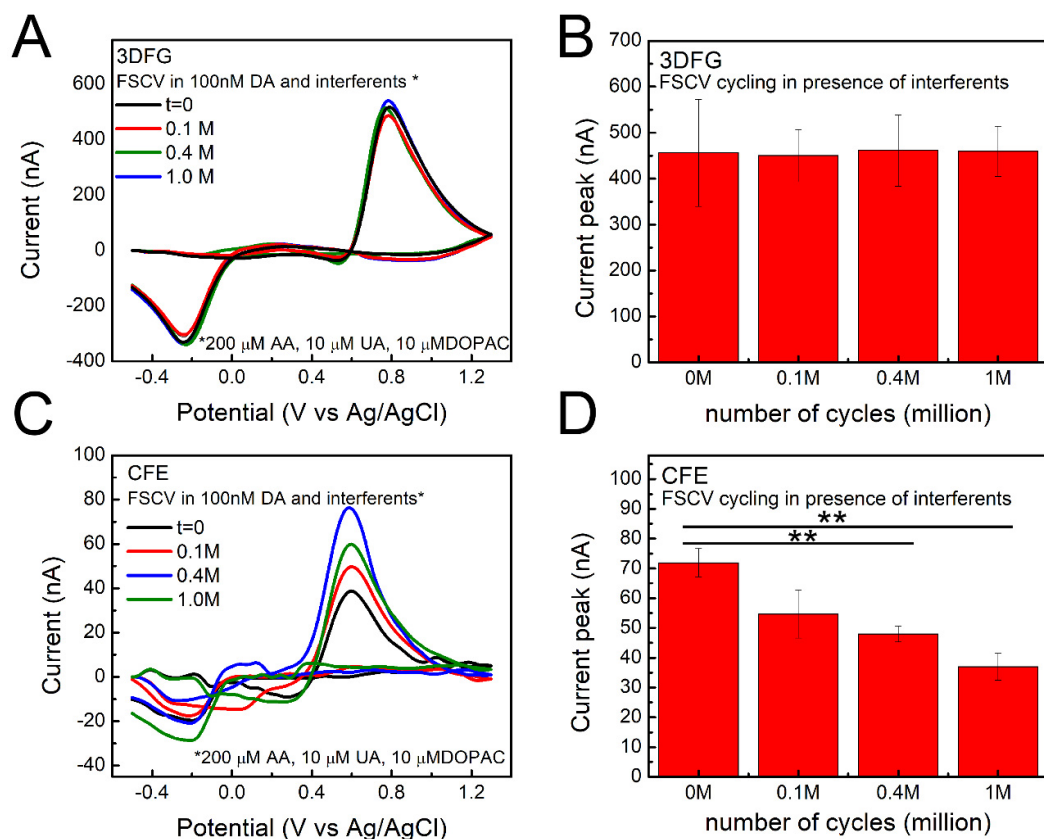
Figure 5. DA sensing stability and fouling properties with 3DFG and CFEs in presence of contaminant. (A, B) 3DFG: **(A)** Representative background subtracted CVs in response to 1μM bolus injections of DA at the time 0 and after 0.1, 0.4 and 1 million (corresponding to 3, 8, and 24 hours) of 3DFG FSCV continuous scanning in PBS containing 100 nM DA and contaminants (200 μM AA, 10 μM UA, 10 μM DOPAC). **(B)** Column plot reporting the amplitude of the oxidation peaks collected in response to 1μM bolus injections of DA at time zero and after 0.1, 0.4 and 0.9 million of 3DFG FSCV continuous scanning in PBS containing 100 nM DA and contaminants (200 μM AA, 10 μM UA, 10 μM DOPAC), (Repeated measurements ANOVA, $F_{(3,12)}=0.05014$, $P=0.98443>0.05$, Bonferroni post-test not stat different, n=3, 5 repetitions) **(C, D)** CFEs: **(C)** Representative background subtracted CVs in response to 1μM bolus injections of DA at the time 0 and after 0.1, 0.4 and 0.9 million of CFE FSCV continuous scanning in PBS containing 100 nM

DA and contaminants (200 μM AA, 10 μM UA, 10 μM DOPAC). **(D)** Column plot reporting the amplitude of the oxidation peaks collected in response to 1μM bolus injections of DA at time zero and after 0.1, 0.4 and 0.9 million of CFE FSCV continuous scanning in PBS containing 100 nM DA and contaminants (200 μM AA, 10 μM UA, 10 μM DOPAC). (Repeated measurements ANOVA, $F_{(3,33)}=9.16405$, $P=1.4835E-4<0.05$, Bonferroni post-test ** stat different, n=3, 5 repetitions).

Finally, we investigated the selectivity of 3DFG in detection of DA over serotonin (5-HT). 5-HT is a cationic indolamine neurotransmitter, and like DA, can be electrochemically oxidized within the physiological pH solvent window (Wrona and Dryhurst 1990) with an oxidation reaction mechanism that involves a multi-step two-electron, two-proton transfer process (Jackson et al. 1995; Patel et al. 2013; Verbiese-Genard et al. 1984).

The detection of 5-HT using FSCV at CFEs is challenging since the by-products formed during the reaction, such as reactive carbocation intermediate and dimers, (Jackson et al. 1995; Patel et al. 2013; Wrona and Dryhurst 1990) are highly reactive and adsorb irreversibly on the electrode surface resulting in electrode fouling. This limitation has been partially solved by the use of optimized FSCV waveforms and/or electrode surface treatments (Swamy and Venton 2007a; Yang et al. 2017; Zestos et al. 2014). The Jackson waveform, (Hashemi et al. 2009; Jackson et al. 1995; Puthongkham and Venton 2020) a N-shaped waveform that holds the potential at +0.2 V to limit 5-HT by-product adsorption and scans quickly at 1000 V/s to 1.0 V and switch down to −0.1 V, allows for the detection of the 5-HT reduction peak (Hashemi et al. 2009; Jackson et al. 1995; Puthongkham and Venton 2020), while accelerating the electrode response times and limiting the fouling. However, such N-shaped FSCV waveforms cannot be effectively used to detect DA since DA sensing requires a more negative holding potential to facilitate the cationic adsorption on the

electrode surface and to detect the DA reduction peak (Swamy and Venton 2007a; Zestos et al. 2014). On the other hand, different high surface area carbon materials(Swamy and Venton 2007a; Yang et al. 2017; Zestos et al. 2014), have been investigated and shown promising fouling resistance to 5-HT reaction byproduct (Mendoza et al. 2020; Swamy and Venton 2007a; Weese et al. 2019; Zestos et al. 2014), which has been mainly attributed to the presence of defect sites in high density (Mendoza et al. 2020; Zestos et al. 2014).

There is a great interest in understanding the interplay between DA and 5-HT release in reward and learning (Balasubramani et al. 2015; Fischer and Ullsperger 2017) and in the progression of neurological disease, such as Parkinson's disease (Boileau et al. 2008; Carta et al. 2008; Politis et al. 2012; Wong et al. 1995), schizophrenia (Kapur and Remington 1996; Niederkofler et al. 2015), and depression (Boileau et al. 2008; Dremencov et al. 2004; Zangen et al. 2001). However, to the best of our knowledge, few studies have reported simultaneous detection of DA and 5-HT via FSCV (Swamy and Venton 2007a; Zestos et al. 2014; Zhou et al. 2005), using bare CFEs (Zhou et al. 2005), CNT coated CFEs (Swamy and Venton 2007a), or CNT fibers (Zestos et al. 2014). In all these cases, DA and 5-HT presented similar oxidation potentials (around 0.6 V) and the microelectrodes were only able to discriminate the reduction peaks of DA and 5-TH, at 200 mV ' (Swamy and Venton 2007a; Zhou et al. 2005) and 400mV respectively (Zestos et al. 2014).

We explored the ability of 3DFG electrodes to simultaneously detect DA and 5-HT using FSCV and we compared their performance (Figure 6 A, B) with bare CFEs (Figure 6 C, D). Using 3DFG microelectrodes, the 5-TH background subtracted CV plot shows two clear oxidation peaks, respectively at ca. 0.51 V and ca. 0.78 V and reduction peak at ca. 0.08 V (Figure 6.B black). Well separated reduction and oxidation peaks of DA and 5-HT in response to the injection of their 50:50 mixture can be identified via color plots (Figure 6 A) and background subtracted CV plots (Figure

6.B). 3DFG detected reduction peaks of DA and 5-HT at -0.22 V and 0.08 V, respectively; and the oxidation peak of 5-HT at 0.51 V, while the second 5-HT oxidation peak at 0.78 V converges with the DA oxidation peak, resulting in a 2-fold greater peak amplitude. In the case of CFEs, only the reduction peaks of DA (-0.18 V) and 5-HT (0.08V) can be distinguished, while the oxidation peaks converged into a single peak at ca. 0.6 V vs. Ag/AgCl (Figure 6.C and D), consistent with the results from previously reported studies (Zhou et al. 2005). The unique capability of 3DFG to distinguish the peak at 0.51 V (likely assigned to the intermediate step of the 5-HT oxidation reaction)(Wrona and Dryhurst 1987), is mainly attributable to its higher sensitivity afforded by the high surface area.

Additionally, we demonstrated the 3DFG ability to simultaneously detect DA and 5-HT using FSCV in the presence of 200 μM AA, 10 μM UA, 10 μM DOPAC and 100 nM DA (Figure 6 E, F). Figure 6.G and H present the color plot and background-subtracted CVs showing reduction and oxidation peaks of DA, injected at 5 s, in the presence of interferents, and the simultaneous detection of DA and 5-HT after subsequent injection of 5-HT at 10 s, showing both oxidation and reduction 5-HT peaks. These results indicate that 3DFG microelectrodes can facilitate the co-detection of DA and 5-HT and can be employed towards quantifying the concentrations of DA and 5-HT simultaneously.
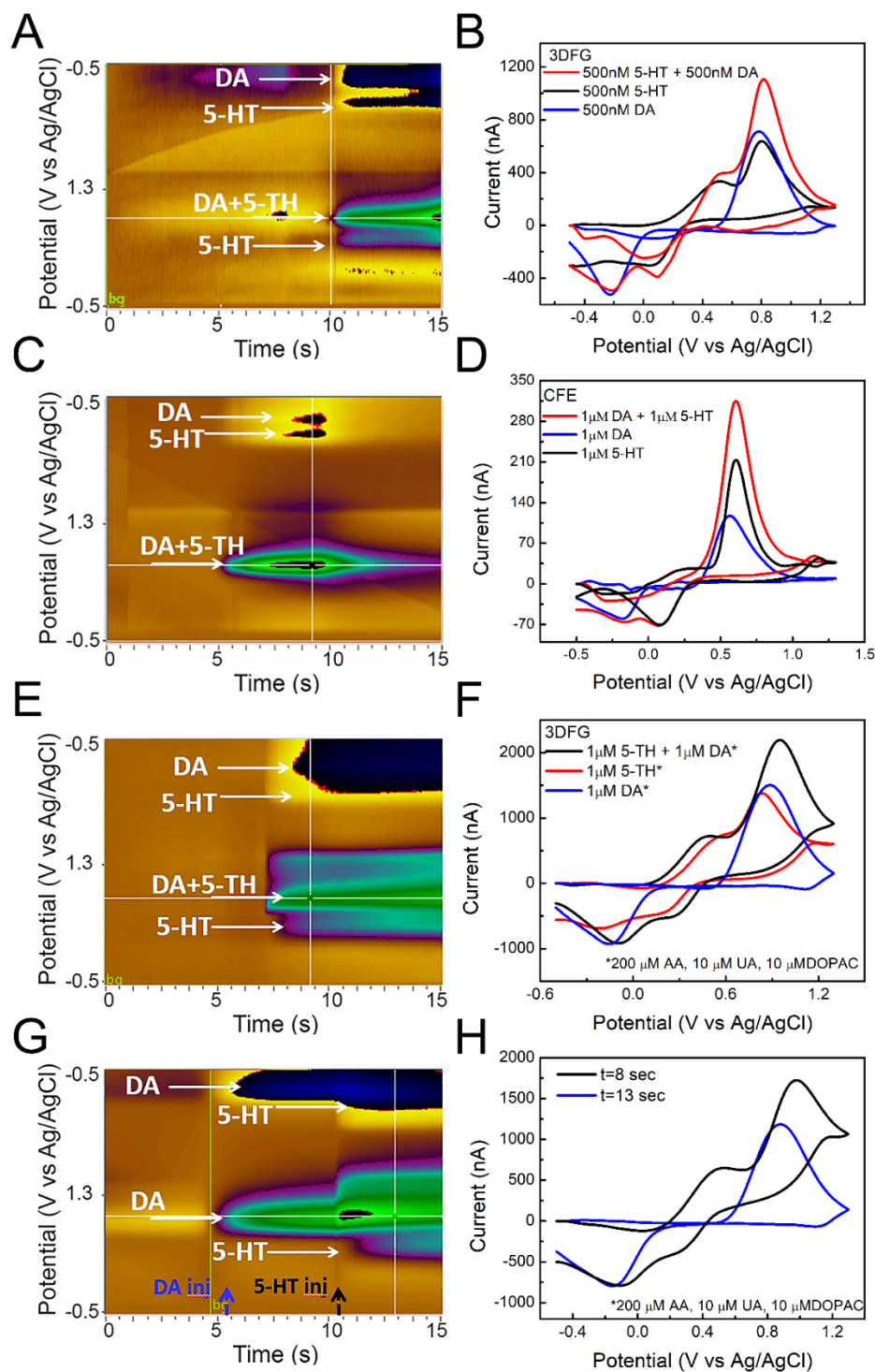
Figure 6. DA and 5-HT simultaneous detection using 3DFG and CFEs. (A,B) 3DFG **(A)** A representative color plot showing clear separation peaks (reduction and oxidation) of DA and 5-HT and **(B)** Background subtracted CVs showing reduction and oxidation peaks of dopamine

(DA), serotonin (5-HT) and their simultaneous detection (50:50% DA and 5-HT) using a standard pyramidal FSCV waveform in which the applied voltage was ramped from the holding potential of −0.5 V to the switching potential of +1.3V and then back to −0.5V at 400 V/s, at 10 Hz. 3DFG can discriminate both reduction and oxisation peaks. **(C,D)** CFEs. **(A)** Color plot for simultaneous DA and 5-HT detection showing showing clear separation only for the reduction peaks. **(D)** Background subtracted CV showing reduction and oxidation peaks of dopamine (DA), serotonin (5-HT) and their simultaneous detection using a standard pyramidal FSCV waveform in which the applied voltage was ramped from the holding potential of −0.5 V to the switching potential of +1.3V and then back to −0.5V at 400 V/s, at 10 Hz. **(E, F)** Representative color plot and background subtracted CVs showing reduction and oxidation peaks of dopamine (DA), serotonin (5-HT) and their simultaneous detection concentration in the presence of 200 μM AA, 10 μM UA, 10 μM DOPAC; DA and 5-HT were injected in a 50:50% mixture and signals were measured using a standard pyramidal FSCV waveform in which the applied voltage was ramped from the holding potential of −0.5 V to the switching potential of +1.3V and then back to −0.5V at 400 V/s, at 10 Hz. 3DFG can discriminate both reduction and oxidation of DA and 5-HT in simultaneous detection also in presence of contaminants. **(G, H)** Color plot and background subtracted CVs showing reduction and oxidation peaks of dopamine (DA, Injected at 5 s), and their simultaneous detection concentration in the presence of contaminants after a subsequent injection of serotonin (5-HT) at 10 s.

4. Conclusions

In this study, we present a high-density MEA platform, with 3DFG microelectrodes, synthetized using a catalyst-free process that enables high control over the materials structure. Using standard micro- and nano-fabrication techniques, the 3DFG can be pattenered into functional microelectrodes with sizes varying from 2 x 2 μm^2 to 50 x 50 μm^2. The EIS and CSC results highlight the ability of the 3DFG to provide acceptable electrochemical performance at ultrasmall size due to the material's high surface area, opening the possibility to fabricate high-density subcellular sized microelectrode arrays. Raman spectroscopy comfirmes a defect-rich, graphene-based nanostructure ideal for neurotransmitter detection (Puthongkham and Venton 2020; Puthongkham et al. 2018; Zestos et al. 2015).

The sensitivity of 50 x 50 μm^2 3DFG microelectrodes is up to 586-fold greater than that reported for CFEs and the highest for nanocarbon microelectrodes using FSCV. The LOD for DA sensing was calculated to be 990±15 pM, the lowest reported using FSCV for carbon-based materials for DA detection. The sensitivity of miniaturized 2 x 2 μm^2 3DFG microelectrodes is comparable to the sensitivity of CFEs with 2200-folder larger geometric area and their LOD was determined to be 3.6 ± 2.2 nM, extremely low for microelectrodes of such dimensions. 3DFG microelectrodes are electrochemically stable under 7.2 million of continuous FSCV cycling, and present exceptional selectivity and fouling resistance to the deposition of byproducts generated by electrochemical reactions, significantly outperforming CFEs in preserving the DA sensitivity over 24 h of continuous FSCV cycling (1 million FSCV scans) in 1x PBS containing 200 μM AA, 10 μM UA, 10 μM DOPAC, and 100 nM DA. Furthermore, 3DFG can discriminate DA and 5-HT in response to the injection of their 50:50 mixture, in 1x PBS and in presence of 200 μM AA, 10 μM

UA, 10 µM DOPAC and 100 nM DA; suggesting that 3DFG microelectrodes can be further investigated for the co-detection of DA and 5-HT.

These results demonstrate that 3DFG microelectrodes present a breakthrough platform for DA sensing using FSCV with high sensitivity, selectivity, and spatial resolution. This study represents the first step, i.e. the sensor optimization, toward the multi-site neurotransmitter measurements for neuroscience studies. Future efforts will include (1) the design of the electronics with an appropriate circuit to allow for multiple-channel FSCV measurements, preventing cross-talks between adjacent microelectrodes, and (2) the implementation of a software platform for data acquisition, real-time visualization, and analysis of the large amount of FSCV data generated from high density microelectrode arrays.

Supporting Information. The Supporting Information is provided as a separate file.

Author Information

*Corresponding author: Tzahi Cohen-Karni tzahi@andrew.cmu.edu, Tracy Cui xic11@pitt.edu

Author Contributions

TCK and XYC conceptualized the project. EC performed the electrochemical characterization and sensing experiments, performed in vitro fouling experiments and data analysis, and wrote the manuscript. RG fabricated part of the 3DFG microelectrode arrays and performed Raman and SEM characterization. SKR fabricated part of the 3DFG microelectrode arrays and conduct electrochemical characterization and SEM imaging. TCK led and supervised the fabrication, and device characterization, edited and revised the manuscript. XYC supervised the sensing experiments, guided the data analysis, and edited and revised the manuscript. All authors contributed to the article and approved the submitted version.

Conflict of Interest Contributions

All authors have no conflict of interest to declare.

References

Ahlskog, J.E., 2007. Beating a dead horse: dopamine and Parkinson disease. Neurology 69(17), 1701-1711 DOI: https://doi.org/1710.1212/1701.wnl.0000296942.0000214309.0000296944a.

Arias-Carrión, Ó., Pöppel, E., 2007. Dopamine, learning, and reward-seeking behavior. Acta neurobiologiae experimentalis.

Atcherley, C.W., Wood, K.M., Parent, K.L., Hashemi, P., Heien, M.L., 2015. The coaction of tonic and phasic dopamine dynamics. Chemical Communications 51(12), 2235-2238 DOI: 2210.1039/C2234CC06165A

Balasubramani, P.P., Chakravarthy, V.S., Ravindran, B., Moustafa, A.A., 2015. A network model of basal ganglia for understanding the roles of dopamine and serotonin in reward-punishment-risk based decision making. Frontiers in computational neuroscience 9, 76 https://doi.org/10.3389/fncom.2015.00076.

Bard, A.J., Faulkner, L.R., 2001. Fundamentals and applications. Electrochemical Methods 2(482), 580-632.

Bath, B.D., Michael, D.J., Trafton, B.J., Joseph, J.D., Runnels, P.L., Wightman, R.M., 2000. Subsecond adsorption and desorption of dopamine at carbon-fiber microelectrodes. Analytical chemistry 72(24), 5994-6002 https://doi.org/5910.1021/ac000849y.

Baur, J.E., Kristensen, E.W., May, L.J., Wiedemann, D.J., Wightman, R.M., 1988. Fast-scan voltammetry of biogenic amines. Analytical chemistry 60(13), 1268-1272 DOI: 1210.1021/ac00164a00006.

Bissett, M.A., Izumida, W., Saito, R., Ago, H., 2012. Effect of domain boundaries on the Raman spectra of mechanically strained graphene. ACS nano 6(11), 10229-10238 https://doi.org/10210.11021/nn304032f.

Bissett, M.A., Tsuji, M., Ago, H., 2014. Strain engineering the properties of graphene and other two-dimensional crystals. Physical Chemistry Chemical Physics 16(23), 11124-11138 DOI: 11110.11039/C11123CP55443K

Boileau, I., Warsh, J.J., Guttman, M., Saint-Cyr, J.A., McCluskey, T., Rusjan, P., Houle, S., Wilson, A.A., Meyer, J.H., Kish, S.J., 2008. Elevated serotonin transporter binding in depressed patients with Parkinson's disease: a preliminary PET study with [11C] DASB. Movement disorders: official journal of the Movement Disorder Society 23(12), 1776-1780 https://doi.org/1710.1002/mds.22212.

Bowling, R., Packard, R.T., McCreery, R.L., 1989. Mechanism of electrochemical activation of carbon electrodes: role of graphite lattice defects. Langmuir 5(3), 683-688 https://doi.org/610.1021/la00087a00022.

Brisch, R., Saniotis, A., Wolf, R., Bielau, H., Bernstein, H.-G., Steiner, J., Bogerts, B., Braun, K., Jankowski, Z., Kumaratilake, J., 2014. The role of dopamine in schizophrenia from a neurobiological and evolutionary perspective: old fashioned, but still in vogue. Frontiers in psychiatry 5, 47 https://doi.org/10.3389/fpsyt.2014.00047.

Cao, Q., Puthongkham, P., Venton, B.J., 2019. new insights into optimizing chemical and 3D surface structures of carbon electrodes for neurotransmitter detection. Analytical Methods 11(3), 247-261 https://doi.org/210.1039/C1038AY02472C.

Cao, Q., Shin, M., Lavrik, N.V., Venton, B.J., 2020. 3D-Printed Carbon Nanoelectrodes for In Vivo Neurotransmitter Sensing. Nano Letters 20(9), 6831–6836 https://doi.org/6810.1021/acs.nanolett.6830c02844.

Carta, M., Carlsson, T., Muñoz, A., Kirik, D., Björklund, A., 2008. Serotonin–dopamine interaction in the induction and maintenance of L-DOPA-induced dyskinesias. Progress in brain research 172, 465-478 DOI: 410.1016/S0079-6123(1008)00922-00929.

Castagnola, E., Vahidi, N.W., Nimbalkar, S., Rudraraju, S., Thielk, M., Zucchini, E., Cea, C., Carli, S., Gentner, T.Q., Ricci, D., 2018. In vivo dopamine detection and single unit recordings using intracortical glassy carbon microelectrode arrays. MRS advances 3(29), 1629 DOI: 1610.1557/adv.2018.1698.

Castagnola, E., Woeppel, K., Golabchi, A., McGuier, M., Chodapaneedi, N., Metro, J., Taylor, I.M., Cui, X.T., 2020. Electrochemical detection of exogenously administered melatonin in the brain. Analyst 145(7), 2612-2620 https://doi.org/2610.1039/D2610AN00051E.

Cogan, S.F., 2008. Neural stimulation and recording electrodes. Annu. Rev. Biomed. Eng. 10, 275-309 DOI: 210.1146/annurev.bioeng.1110.061807.160518.

Dremencov, E., Gispan-Herman, I., Rosenstein, M., Mendelman, A., Overstreet, D.H., Zohar, J., Yadid, G., 2004. The serotonin–dopamine interaction is critical for fast-onset action of antidepressant treatment: in vivo studies in an animal model of depression. Progress in Neuro-Psychopharmacology and Biological Psychiatry 28(1), 141-147 DOI: 110.1016/j.pnpbp.2003.1009.1030

DuVall, S.H., McCreery, R.L., 2000. Self-catalysis by catechols and quinones during heterogeneous electron transfer at carbon electrodes. Journal of the American Chemical Society 122(28), 6759-6764 https://doi.org/6710.1021/ja000227u.

El Merhie, A., Ito, D., Colombi, I., Keshavan, S., Mishra, N., Miseikis, V., Diaspro, A., Coletti, C., Chiappalone, M., Dante, S., 2018. Single layer graphene functionalized MEA for enhanced detection of neuronal network development. Sensors and Actuators B: Chemical 277, 224-233 https://doi.org/210.1016/j.snb.2018.1008.1142.

Engstrom, R.C., Strasser, V.A., 1984. Characterization of electrochemically pretreated glassy carbon electrodes. Analytical Chemistry 56(2), 136-141 https://doi.org/110.1021/ac00266a00005.

Ferrari, A.C., Basko, D.M., 2013. Raman Spectroscopy as a Versatile Tool for Studying the Properties of Graphene. Nature Nanotechnology 8(4), 235 https://doi.org/210.1038/nnano.2013.1046.

Fischer, A.G., Ullsperger, M., 2017. An update on the role of serotonin and its interplay with dopamine for reward. Frontiers in human neuroscience 11, 484 https://doi.org/410.3389/fnhum.2017.00484.

Forster, R.J., 1994. Microelectrodes: new dimensions in electrochemistry. Chemical Society Reviews 23(4), 289-297 https://doi.org/210.1039/CS9942300289.

Forster, R.J., 2006. Ultrafast electrochemical techniques. Encyclopedia of Analytical Chemistry: Applications, Theory and Instrumentation, https://doi.org/10.1002/9780470027318.a9780470025319.pub9780470027312.

Garg, R., Rastogi, S.K., Lamparski, M., de la Barrera, S.C., Pace, G.T., Nuhfer, N.T., Hunt, B.M., Meunier, V., Cohen-Karni, T., 2017. Nanowire-mesh-templated growth of out-of-plane three-dimensional fuzzy graphene. ACS nano 11(6), 6301-6311 https://doi.org/6310.1021/acsnano.6307b02612.

Goshi, N., Castagnola, E., Vomero, M., Gueli, C., Cea, C., Zucchini, E., Bjanes, D., Maggiolini, E., Moritz, C., Kassegne, S., 2018. Glassy carbon MEMS for novel origami-styled 3D integrated intracortical and epicortical neural probes. Journal of Micromechanics and Microengineering 28(6), 065009 https://doi.org/065010.061088/061361-066439/aab065061.

Gründer, G., Cumming, P., 2016. The dopamine hypothesis of schizophrenia: Current status. The Neurobiology of Schizophrenia, pp. 109-124 110.1016/B1978-1010-1012-801829-801823.800015-X. Elsevier.

Hanssen, B.L., Siraj, S., Wong, D.K., 2016. Recent strategies to minimise fouling in electrochemical detection systems. Reviews in Analytical Chemistry 35(1), 1-28 DOI 10.1515/revac-2015-0008.

Harreither, W., Trouillon, R., Poulin, P., Neri, W., Ewing, A.G., Safina, G., 2016. Cysteine residues reduce the severity of dopamine electrochemical fouling. Electrochimica Acta 210, 622-629 610.1016/j.electacta.2016.1005.1124.

Harris, D.C., 2010. Quantitative chemical analysis. Macmillan.

Hashemi, P., Dankoski, E.C., Petrovic, J., Keithley, R.B., Wightman, R., 2009. Voltammetric detection of 5-hydroxytryptamine release in the rat brain. Analytical chemistry 81(22), 9462-9471 https://doi.org/9410.1021/ac9018846.

Heien, M.L., Phillips, P.E., Stuber, G.D., Seipel, A.T., Wightman, R.M., 2003. Overoxidation of carbon-fiber microelectrodes enhances dopamine adsorption and increases sensitivity. Analyst 128(12), 1413-1419 https://doi.org/1410.1039/B307024G.

Hensley, A.L., Colley, A.R., Ross, A.E., 2018. Real-Time Detection of Melatonin Using Fast-Scan Cyclic Voltammetry. Analytical chemistry 90(14), 8642-8650 DOI: 8610.1021/acs.analchem.8648b01976.

Höglinger, G.U., Rizk, P., Muriel, M.P., Duyckaerts, C., Oertel, W.H., Caille, I., Hirsch, E.C., 2004. Dopamine depletion impairs precursor cell proliferation in Parkinson disease. Nature neuroscience 7(7), 726-735 DOI: 710.1038/nn1265.

Howe, M.W., Tierney, P.L., Sandberg, S.G., Phillips, P.E., Graybiel, A.M., 2013. Prolonged dopamine signalling in striatum signals proximity and value of distant rewards. nature 500(7464), 575-579 510.1038/nature12475.

Jackson, B.P., Dietz, S.M., Wightman, R.M., 1995. Fast-scan cyclic voltammetry of 5-hydroxytryptamine. Analytical chemistry 67(6), 1115-1120 https://doi.org/1110.1021/ac00102a00015.

Johnson, J.A., Rodeberg, N.T., Wightman, R.M., 2018. Measurement of basal neurotransmitter levels using convolution-based nonfaradaic current removal. Analytical chemistry 90(12), 7181-7189 https://doi.org/7110.1021/acs.analchem.7187b04682.

Kapur, S., Remington, G., 1996. Serotonin-dopamine interaction and its relevance to schizophrenia. American Journal of Psychiatry 153(4), 466-476 DOI: 410.1176/ajp.1153.1174.1466.

Kim, D.H., Oh, Y., Shin, H., Park, C., Blaha, C.D., Bennet, K.E., Kim, I.Y., Lee, K.H., Jang, D.P., 2018. Multi-waveform fast-scan cyclic voltammetry mapping of adsorption/desorption kinetics of biogenic amines and their metabolites. Analytical Methods 10(24), 2834-2843 https://doi.org/2810.1039/C2838AY00352A.

Liu, X., Ren, C., Lu, Y., Hattori, R., Shi, Y., Zhao, R., Ding, D., Komiyama, T., Kuzum, D., 2019. Decoding ECoG High Gamma Power from Cellular Calcium Response using Transparent Graphene Microelectrodes. 2019 9th International IEEE/EMBS Conference on Neural Engineering (NER), pp. 710-713 DOI: 710.1109/NER.2019.8717147. IEEE.

Lotharius, J., Brundin, P., 2002. Pathogenesis of Parkinson's disease: dopamine, vesicles and α-synuclein. Nature Reviews Neuroscience 3(12), 932-942 https://doi.org/910.1038/nrn1983.

Lu, Y., Liu, X., Hattori, R., Ren, C., Zhang, X., Komiyama, T., Kuzum, D., 2018. Ultralow Impedance Graphene Microelectrodes with High Optical Transparency for Simultaneous Deep Two-Photon Imaging in Transgenic Mice. Advanced Functional Materials 28(31), 1800002 https://doi.org/1800010.1801002/adfm.201800002.

McCreery, R.L., 2008. Advanced carbon electrode materials for molecular electrochemistry. Chemical reviews 108(7), 2646-2687 https://doi.org/2610.1021/cr068076m.

McDermott, M.T., McCreery, R.L., 1994. Scanning tunneling microscopy of ordered graphite and glassy carbon surfaces: electronic control of quinone adsorption. Langmuir 10(11), 4307-4314 https://doi.org/4310.1021/ac00055a00017.

Mendoza, A., Asrat, T., Liu, F., Wonnenberg, P., Zestos, A.G., 2020. Carbon Nanotube Yarn Microelectrodes Promote High Temporal Measurements of Serotonin Using Fast Scan Cyclic Voltammetry. Sensors 20(4), 1173.

Mohebi, A., Pettibone, J.R., Hamid, A.A., Wong, J.-M.T., Vinson, L.T., Patriarchi, T., Tian, L., Kennedy, R.T., Berke, J.D., 2019. Dissociable dopamine dynamics for learning and motivation. Nature 570(7759), 65-70.

Niederkofler, V., Asher, T.E., Dymecki, S.M., 2015. Functional interplay between dopaminergic and serotonergic neuronal systems during development and adulthood. ACS chemical neuroscience 6(7), 1055-1070 https://doi.org/1010.1021/acschemneuro.1055b00021.

Nimbalkar, S., Castagnola, E., Balasubramani, A., Scarpellini, A., Samejima, S., Khorasani, A., Boissenin, A., Thongpang, S., Moritz, C., Kassegne, S., 2018. Ultra-capacitive carbon neural probe allows simultaneous long-term electrical stimulations and high-resolution neurotransmitter detection. Scientific reports 8(1), 1-14 https://doi.org/10.1038/s41598-41018-25198-x.

Oh, Y., Heien, M.L., Park, C., Kang, Y.M., Kim, J., Boschen, S.L., Shin, H., Cho, H.U., Blaha, C.D., Bennet, K.E., 2018. Tracking tonic dopamine levels in vivo using multiple cyclic square

wave voltammetry. Biosensors and Bioelectronics 121, 174-182 https://doi.org/110.1016/j.bios.2018.1008.1034.

Ou, Y., Buchanan, A.M., Witt, C.E., Hashemi, P., 2019. Frontiers in electrochemical sensors for neurotransmitter detection: towards measuring neurotransmitters as chemical diagnostics for brain disorders. Analytical Methods 11(21), 2738-2755 DOI: 2710.1039/C2739AY00055K.

Owesson-White, C.A., Ariansen, J., Stuber, G.D., Cleaveland, N.A., Cheer, J.F., Mark Wightman, R., Carelli, R.M., 2009. Neural encoding of cocaine-seeking behavior is coincident with phasic dopamine release in the accumbens core and shell. European Journal of Neuroscience 30(6), 1117-1127 https://doi.org/1110.1111/j.1460-9568.2009.06916.x.

Pancrazio, J.J., Deku, F., Ghazavi, A., Stiller, A.M., Rihani, R., Frewin, C.L., Varner, V.D., Gardner, T.J., Cogan, S.F., 2017. Thinking small: Progress on microscale neurostimulation technology. Neuromodulation: Technology at the Neural Interface 20(8), 745-752.

Patel, A.N., Unwin, P.R., Macpherson, J.V., 2013. Investigation of film formation properties during electrochemical oxidation of serotonin (5-HT) at polycrystalline boron doped diamond. Physical Chemistry Chemical Physics 15(41), 18085-18092 DOI: 18010.11039/C18083CP53513D

Phillips, P.E., Stuber, G.D., Heien, M.L., Wightman, R.M., Carelli, R.M., 2003. Subsecond dopamine release promotes cocaine seeking. Nature 422(6932), 614-618 https://doi.org/610.1038/nature01476.

Politis, M., Wu, K., Loane, C., Quinn, N.P., Brooks, D.J., Oertel, W.H., Björklund, A., Lindvall, O., Piccini, P., 2012. Serotonin neuron loss and nonmotor symptoms continue in Parkinson's patients treated with dopamine grafts. Science translational medicine 4(128), 128ra141-128ra141 DOI: 110.1126/scitranslmed.3003391.

Poon, M., McCreery, R.L., Engstrom, R., 1988. Laser activation of carbon electrodes. Relationship between laser-induced surface effects and electron transfer activation. Analytical Chemistry 60(17), 1725-1730 https://doi.org/1710.1021/ac00168a00018.

Puthongkham, P., Venton, B.J., 2020. Recent Advances in Fast-Scan Cyclic Voltammetry. Analyst 145, 1087-1102 DOI: 1010.1039/C1089AN01925A.

Puthongkham, P., Yang, C., Venton, B.J., 2018. Carbon Nanohorn-modified Carbon Fiber Microelectrodes for Dopamine Detection. Electroanalysis 30(6), 1073-1081 https://doi.org/1010.1002/elan.201700667.

Rastogi, S.K., Bliley, J., Matino, L., Garg, R., Santoro, F., Feinberg, A.W., Cohen-Karni, T., 2020. Three-dimensional fuzzy graphene ultra-microelectrodes for subcellular electrical recordings. Nano Research 13(5), 1444-1452 https://doi.org/1410.1007/s12274-12020-12695-y.

Rastogi, S.K., Bliley, J., Shiwarski, D.J., Raghavan, G., Feinberg, A.W., Cohen-Karni, T., 2018. Graphene microelectrode arrays for electrical and optical measurements of human stem cell-derived cardiomyocytes. Cellular and Molecular Bioengineering 11(5), 407-418 https://doi.org/410.1007/s12195-12018-10525-z.

Rees, H.R., Anderson, S.E., Privman, E., Bau, H.H., Venton, B.J., 2015. Carbon nanopipette electrodes for dopamine detection in Drosophila. Analytical chemistry 87(7), 3849-3855 https://doi.org/3810.1021/ac504596y.

Roitman, M.F., Stuber, G.D., Phillips, P.E., Wightman, R.M., Carelli, R.M., 2004. Dopamine operates as a subsecond modulator of food seeking. Journal of Neuroscience 24(6), 1265-1271 DOI: https://doi.org/1210.1523/JNEUROSCI.3823-1203.2004.

San Roman, D., Krishnamurthy, D., Garg, R., Hafiz, H., Lamparski, M., Nuhfer, N.T., Meunier, V., Viswanathan, V., Cohen-Karni, T., 2020. Engineering three-dimensional (3D) out-of-plane graphene edge sites for highly selective two-electron oxygen reduction electrocatalysis. ACS Catalysis 10(3), 1993-2008 https://doi.org/1910.1021/acscatal.1999b03919.

Schmidt, A.C., Wang, X., Zhu, Y., Sombers, L.A., 2013. Carbon nanotube yarn electrodes for enhanced detection of neurotransmitter dynamics in live brain tissue. ACS nano 7(9), 7864-7873 https://doi.org/7810.1021/nn402857u.

Schultz, W., 2007. Multiple dopamine functions at different time courses. Annu. Rev. Neurosci. 30, 259-288 https://doi.org/210.1146/annurev.neuro.1128.061604.135722.

Schwerdt, H.N., Shimazu, H., Amemori, K.-i., Amemori, S., Tierney, P.L., Gibson, D.J., Hong, S., Yoshida, T., Langer, R., Cima, M.J., 2017. Long-term dopamine neurochemical monitoring in primates. Proceedings of the National Academy of Sciences 114(50), 13260-13265 https://doi.org/13210.11073/pnas.1713756114.

Schwerdt, H.N., Zhang, E., Kim, M.J., Yoshida, T., Stanwicks, L., Amemori, S., Dagdeviren, H.E., Langer, R., Cima, M.J., Graybiel, A.M., 2018. Cellular-scale probes enable stable chronic subsecond monitoring of dopamine neurochemicals in a rodent model. Communications biology 1(1), 1-11 https://doi.org/10.1038/s42003-42018-40147-y.

Seven, F., Gölcez, T., Mustafa, Ş., 2020. Nanoporous carbon-fiber microelectrodes for sensitive detection of H2O2 and dopamine. Journal of Electroanalytical Chemistry 114104 DOI: 114110.111016/j.jelechem.112020.114104.

Si, B., Song, E., 2018. Recent advances in the detection of neurotransmitters. Chemosensors 6(1), 1 https://doi.org/10.3390/chemosensors6010001.

Smith, S.K., Gosrani, S.P., Lee, C.A., McCarty, G.S., Sombers, L.A., 2018. Carbon-fiber microbiosensor for monitoring rapid lactate fluctuations in brain tissue using fast-scan cyclic voltammetry. Analytical chemistry 90(21), 12994-12999 https://doi.org/12910.11021/acs.analchem.12998b03694.

Stouffer, M.A., Woods, C.A., Patel, J.C., Lee, C.R., Witkovsky, P., Bao, L., Machold, R.P., Jones, K.T., De Vaca, S.C., Reith, M.E., 2015. Insulin enhances striatal dopamine release by activating cholinergic interneurons and thereby signals reward. Nature communications 6, 8543 DOI: 8510.1038/ncomms9543.

Swamy, B.K., Venton, B.J., 2007a. Carbon nanotube-modified microelectrodes for simultaneous detection of dopamine and serotonin in vivo. Analyst 132(9), 876-884 https://doi.org/810.1039/B705552H.

Swamy, B.K., Venton, B.J., 2007b. Subsecond detection of physiological adenosine concentrations using fast-scan cyclic voltammetry. Analytical chemistry 79(2), 744-750 DOI: 710.1021/ac061820i.

Takmakov, P., Zachek, M.K., Keithley, R.B., Walsh, P.L., Donley, C., McCarty, G.S., Wightman, R.M., 2010. Carbon microelectrodes with a renewable surface. Analytical chemistry 82(5), 2020-2028 https://doi.org/2010.1021/ac902753x.

Taylor, I.M., Patel, N.A., Freedman, N.C., Castagnola, E., Cui, X.T., 2019. Direct in Vivo Electrochemical Detection of Resting Dopamine Using Poly (3, 4-ethylenedioxythiophene)/Carbon Nanotube Functionalized Microelectrodes. Analytical chemistry 91(20), 12917-12927 https://doi.org/12910.11021/acs.analchem.12919b02904.

Taylor, I.M., Robbins, E.M., Catt, K.A., Cody, P.A., Happe, C.L., Cui, X.T., 2017. Enhanced dopamine detection sensitivity by PEDOT/graphene oxide coating on in vivo carbon fiber electrodes. Biosensors and Bioelectronics 89, 400-410 doi: 410.1016/j.bios.2016.1005.1084.

Torrisi, F., Hasan, T., Wu, W., Sun, Z., Lombardo, A., Kulmala, T.S., Hsieh, G.-W., Jung, S., Bonaccorso, F., Paul, P.J., 2012. Inkjet-printed graphene electronics. ACS Nano 6(4), 2992-3006 https://doi.org/2910.1021/nn2044609.

Venton, B.J., Cao, Q., 2020. Fundamentals of fast-scan cyclic voltammetry for dopamine detection. Analyst 145(4), 1158-1168 https://doi.org/1110.1039/C1159AN01586H.

Verbiese-Genard, N., Kauffmann, J., Hanocq, M., Molle, L., 1984. Study of the electrooxidative behaviour of 5-hydroxyindole-3-acetic acid, 5-hydroxytryptophan and serotonine in the presence of sodium ethylenediaminetetraacetic acid. Journal of electroanalytical chemistry and interfacial electrochemistry 170(1-2), 243-254 https://doi.org/210.1016/0022-0728(1084)80047-80049.

Volkow, N.D., Wang, G.-J., Fowler, J.S., Tomasi, D., Telang, F., 2011. Addiction: beyond dopamine reward circuitry. Proceedings of the National Academy of Sciences 108(37), 15037-15042 https://doi.org/15010.11073/pnas.1010654108.

Vomero, M., Castagnola, E., Ciarpella, F., Maggiolini, E., Goshi, N., Zucchini, E., Carli, S., Fadiga, L., Kassegne, S., Ricci, D., 2017. Highly stable glassy carbon interfaces for long-term neural stimulation and low-noise recording of brain activity. Scientific reports 7(1), 1-14 doi: 10.1038/srep40332 (42017).

Vreeland, R.F., Atcherley, C.W., Russell, W.S., Xie, J.Y., Lu, D., Laude, N.D., Porreca, F., Heien, M.L., 2015. Biocompatible PEDOT: Nafion composite electrode coatings for selective detection of neurotransmitters in vivo. Analytical chemistry 87(5), 2600-2607 DOI: 2610.1021/ac502165f.

Weese, M.E., Krevh, R.A., Li, Y., Alvarez, N.T., Ross, A.E., 2019. Defect sites modulate fouling resistance on carbon-nanotube fiber electrodes. ACS sensors 4(4), 1001-1007 https://doi.org/1010.1021/acssensors.1009b00161.

Wise, R.A., 2004. Dopamine, learning and motivation. Nature reviews neuroscience 5(6), 483-494 https://doi.org/410.1038/nrn1406.

Wong, P.-H., Feng, H., Teo, W., 1995. Interaction of the dopaminergic and serotonergic systems in the rat striatum: effects of selective antagonists and uptake inhibitors. Neuroscience research 23(1), 115-119 https://doi.org/110.1016/0168-0102(1095)90023-90023.

Wrona, M.Z., Dryhurst, G., 1987. Oxidation chemistry of 5-hydroxytryptamine. 1. Mechanism and products formed at micromolar concentrations. The Journal of Organic Chemistry 52(13), 2817-2825 https://doi.org/2810.1021/jo00389a00032.

Wrona, M.Z., Dryhurst, G., 1990. Electrochemical oxidation of 5-hydroxytryptamine in aqueous solution at physiological pH. Bioorganic Chemistry 18(3), 291-317 https://doi.org/210.1016/0045-2068(1090)90005-P.

Yang, C., Jacobs, C.B., Nguyen, M.D., Ganesana, M., Zestos, A.G., Ivanov, I.N., Puretzky, A.A., Rouleau, C.M., Geohegan, D.B., Venton, B.J., 2016a. Carbon nanotubes grown on metal microelectrodes for the detection of dopamine. Analytical chemistry 88(1), 645-652 https://doi.org/610.1021/acs.analchem.1025b01257.

Yang, C., Trikantzopoulos, E., Jacobs, C.B., Venton, B.J., 2017. Evaluation of carbon nanotube fiber microelectrodes for neurotransmitter detection: Correlation of electrochemical performance and surface properties. Analytica chimica acta 965, 1-8 doi: 10.1016/j.aca.2017.1001.1039.

Yang, C., Trikantzopoulos, E., Nguyen, M.D., Jacobs, C.B., Wang, Y., Mahjouri-Samani, M., Ivanov, I.N., Venton, B.J., 2016b. Laser treated carbon nanotube yarn microelectrodes for rapid and sensitive detection of dopamine in vivo. ACS sensors 1(5), 508-515 https://doi.org/510.1021/acssensors.1026b00021.

Yang, W., Ratinac, K.R., Ringer, S.P., Thordarson, P., Gooding, J.J., Braet, F., 2010. Carbon nanomaterials in biosensors: should you use nanotubes or graphene? Angewandte Chemie International Edition 49(12), 2114-2138 DOI: 2110.1002/anie.200903463.

Zachek, M.K., Park, J., Takmakov, P., Wightman, R.M., McCarty, G.S., 2010. Microfabricated FSCV-compatible microelectrode array for real-time monitoring of heterogeneous dopamine release. Analyst 135(7), 1556-1563 https://doi.org/1510.1039/C1550AN00114G.

Zangen, A., Nakash, R., Overstreet, D.H., Yadid, G., 2001. Association between depressive behavior and absence of serotonin–dopamine interaction in the nucleus accumbens. Psychopharmacology 155(4), 434-439 https://doi.org/410.1007/s002130100746.

Zestos, A.G., Jacobs, C.B., Trikantzopoulos, E., Ross, A.E., Venton, B.J., 2014. Polyethylenimine carbon nanotube fiber electrodes for enhanced detection of neurotransmitters. Analytical chemistry 86(17), 8568-8575 https://doi.org/8510.1021/ac5003273.

Zestos, A.G., Yang, C., Jacobs, C.B., Hensley, D., Venton, B.J., 2015. Carbon nanospikes grown on metal wires as microelectrode sensors for dopamine. Analyst 140(21), 7283-7292 DOI: 7210.1039/C7285AN01467K.

Zhou, F.-M., Liang, Y., Salas, R., Zhang, L., De Biasi, M., Dani, J.A., 2005. Corelease of dopamine and serotonin from striatal dopamine terminals. Neuron 46(1), 65-74 https://doi.org/10.1016/j.neuron.2005.1002.1010.